Enhanced Stability of the Metal–Organic Framework MIL-101(Cr) by Embedding Pd Nanoparticles for Densification through Compression

Anna Celeste, Francesco Capitani, Pierre Fertey, Annalisa Paolone, Ferenc Borondics, Oana Grad, Gabriela Blanita, Claudia Zlotea

Enhanced Stability of the Metal-Organic Framework MIL-101(Cr) by Embedding Pd Nanoparticles for Densification Through Compression

Anna Celeste[1,2], Francesco Capitani[2], Pierre Fertey[2], Annalisa Paolone[3], Ferenc Borondics[2], Oana Grad[4], Gabriela Blanita[4], Claudia Zlotea[1]**

1 Institut de Chimie et des Matériaux Paris-Est, CNRS UMR 7182, UPEC, 2-8, rue Henri Dunant, 94320 Thiais, France;

2 Synchrotron SOLEIL, L'Orme des Merisiers, Saint-Aubin, 91192 Gif sur Yvette Cedex, France;

3 Consiglio Nazionale delle Ricerche – Istituto dei Sistemi Complessi, U.O.S. La Sapienza, Piazzale A. Moro 5, 00185 Rome, Italy;

4 National Institute for Research and Development of Isotopic and Molecular Technologies, 67-103 Donat Str., RO-400293 Cluj-Napoca, Romania

Corresponding Authors

*francesco.capitani@synchrotron-soleil.fr * claudia.zlotea@icmpe.cnrs.fr

ABSTRACT

Metal-organic frameworks (MOFs) are ideal platforms for new and original functionalization as the confinement of metallic nanoparticles (NPs) within their pores. However, the insertion of NPs could impact the framework's mechanical stability thus affecting their performances in applications. Indeed, MOFs are usually loose powders that needs to be compressed to increase the volumetric density before to be employed as gas absorbers. Here, we investigate the high-pressure behavior of the mesoporous MOF MIL-101 loaded with Pd NPs (20, 35 wt%) by synchrotron X-ray diffraction and infrared spectroscopy. The control of the metal content allows us to demonstrate that Pd NPs enhance the mechanical stability of MIL-101, with a bulk modulus and a crystalline-amorphous transition pressure increasing with the Pd loading. This is attributed to the NPs steric hindrance whereas the presence of host-guest chemical interactions is ruled out by infrared spectroscopy. We also define a spectroscopic quantity highlighting the framework amorphization, that can be exploited from now on to characterize these materials when densified. Our results demonstrate that the incorporation of NPs makes MOFs not only more functional but also more mechanically stable thus suitable for densification.

TABLE OF CONTENTS

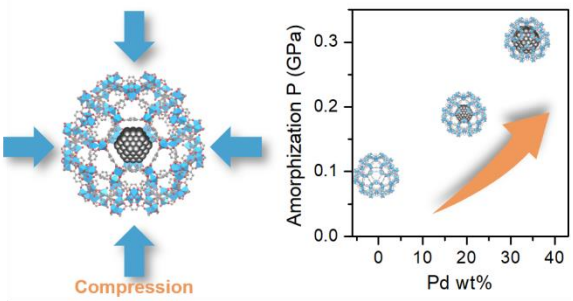

INTRODUCTION

Metal-organic frameworks are extremely versatile porous materials which, with their exceptionally high surface areas and chemical tunability[1], have found application in several domains, from gas adsorption[2] to drug delivery.[3] This success has been possible through the synthesis of chemically and thermally stable frameworks, allowing their use in reactive environments and at relatively high temperature, up to several hundreds of degrees Celsius.[4,5] However, the large extent of voids in the MOFs structure makes these systems prone to mechanical instabilities when submitted to an external stress.[6–8] Previous studies have shown that several effects of fundamental interest emerge in microporous MOFs under pressure, from the most common ones as loss of crystallinity and pore collapse,[6] to more unusual responses as negative linear compressibility and reversible pore closing.[9–11] Evaluating how these materials behave when compressed is important for industrial applications as well. Indeed, common synthetic techniques provide MOFs as powders with low density, technically unsuitable for applications. Increasing the material's density and consequently its mechanical strength, has thus become an important research direction.[12] The densification of MOFs into the form of pellets or monoliths has been achieved through various processes, such as mechanical/hydraulic pressing, extrusion, granulation and some densified MOFs have shown improved volumetric adsorption capacities and separation performances.[13–17] MOFs monoliths are also easier to handle and present high mass transfer rates,[18,19] which is particularly beneficial for gas sorption applications and catalytic reactions.

For these reasons, we previously investigated the high-pressure response of one of the most studied mesoporous MOFs, MIL-101(Cr), pointing out the occurrence of pressure-induced amorphization and the incorporation of a large silicone polymer into the pores (diameters of 29

and 34 Å) at high pressure.[20] Mesoporous MOFs are of particular interest for the encapsulation of guests as molecules[21] or nanoparticles[22] at ambient conditions, opening the way for new composites combining the advantages of both parent materials. In particular, metallic nanoparticles (NPs) have been successfully embedded in several MOFs boosting their performances for hydrogen storage[23,24], catalysis[25] and gas sensing[26], among others.[27]

MIL-101(Cr) has ideal textural properties, thermal and chemical stability for nanoparticles (NPs) confinement. Various metals (Au, Cu, Pt, Ni and Pd) have been inserted in its pores with different metal loadings and nanoparticle sizes.[27–29] Among all metals, Pd is one of the most studied for its unique property to absorb hydrogen at ambient conditions forming an interstitial hydride $PdH_{0.7}$[30] and its interesting catalytic properties in several hydrogenation reactions.[31] Moreover, confining Pd NPs within the pores is a straightforward way to functionalize MOFs and boost their performance.[32,33]

It is worth noting that the NPs confinement is usually confirmed by indirect observations such as a NPs size distribution lower than the pore diameter and the decrease of the internal surface area after the insertion.[34,35] Very rarely, direct observations by electron tomography have been reported, e. g. Ag clusters dispersed inside the pores of MOF-508.[36] However, important artifacts are introduced by this technique (MOF damage by the electron beam and NPs agglomeration) hindering a systematic application of electron tomography.

A new alternative way to confirm the NPs insertion could be to evaluate the framework structural response to external compression which, if affected by the NPs content, would confirm their presence within the pores. The mechanical stability of NPs@MOF composites has never been investigated before and little is known about the capacity of these materials to sustain the densification processes necessary to spread their application.

In this paper, we report for the first time the high-pressure response of MIL-101 with embedded Pd NPs, namely x-Pd@MIL-101 (x=20, 35 wt%), exploiting synchrotron X-ray diffraction (XRD) and infrared (IR) spectroscopy to investigate the effect of the presence of Pd NPs on the mechanical properties of the framework.

EXPERIMENTAL

The pristine MIL-101 $[(Cr_3O)Cl_x(OH)_{1-x}(H_2O)_2(O_2C\text{-}C_6H_4\text{-}CO_2)_3](H_2O)_n$ was synthesized from terephthalic acid, chromium chloride hexahydrate and water, as previously described.[20,37] The obtained powder was activated by heating under reflux with ethanol for 24 hours, filtered and dried at 423 K for 10 hours.

The insertion of Pd nanoparticles (NPs), with loading rates of 20 and 35 wt%, into the MIL-101(Cr) pores was done through a bottom-up double solvent method based on the impregnation of the pristine sample by a precursor solution followed by reduction under Ar/H_2 flow. This procedure is schematically reported in Figure 1 (steps 1-3). We already reported the successful loading of MIL-101 with 20 wt% of Pd NPs (20-Pd@MIL-101).[24,34] For the highest loading, 35 wt%, we employed a slightly modified approach, *i.e.* two consecutive impregnations were performed as detailed below. MIL-101 was first degassed under vacuum (around 10^{-5} mbar) at 493 K for 18 h and 150 mg of degassed MOF were ultrasonicated in 30 mL of pentane for 20 minutes minimizing the exposure of the powder to air. The solution was stirred for 30 minutes and 0.2 mL of an aqueous solution containing H_2PdCl_4 ($1.56x10^{-3}$ mol/mL of Pd) has been added (see step 2 of Figure 1). Thereafter, the mixture was vigorously stirred, in a beaker covered by a parafilm, for 4 hours at room temperature and further stirred without parafilm to let the solvents evaporate. The recovered solid was dried overnight at 343 K in an oven and degassed again in the same conditions already

mentioned. A second impregnation, identical to the first, was performed and finally the recovered powder was reduced under Ar/H_2 flow (0.5 L/min) at 573 K for 15 minutes, as shown in step 3 of Figure 1. This composite will be called 35-Pd@MIL-101 in the following. The presence of randomly dispersed Pd NPs in both composites has been confirmed by Transmission Electron Microscopy (TEM) with a 200 kV FEG TEM (FEI Tecnai F20 equipped with a Gatan Energy Imaging Filter, resolution 0.24 nm) and the average size has been determined through a statistical analysis on several TEM images. Inductively coupled plasma optical emission spectroscopy (ICP-OES) was performed to determine the Pd chemical composition of the composites, resulting in the final values of 19.9±0.5 and 35.0±0.9 wt% of Pd over the whole composite mass for 20-Pd@MIL-101 and 35-Pd@MIL-101 samples, respectively.

The textural properties of MIL-101, 20-Pd@MIL-101 and 35-Pd@MIL-101 were determined from N_2 adsorption-desorption isotherms at 77 K, following the standard BET procedure on the Sorptomatic 1990 (Thermo Electron Corporation, USA) instrument. It is important to stress that all the samples were stored and manipulated in a glovebox under Ar or N_2 gas atmosphere (O_2 and H_2O levels < 1 ppm) and never exposed to air avoiding both water adsorption and Pd NPs oxidation. Moreover, samples were degassed again before every experiment to ensure the removal of possibly adsorbed guest molecules.

High-pressure (HP) XRD and IR data were collected at the SOLEIL Synchrotron (France) at the CRISTAL and SMIS beamlines, respectively. The pressure was generated by a membrane diamond anvil cell (DAC) sketched in Figure 1 (step 5) equipped with 500 µm culet IIas diamonds. Stainless steel gaskets pre-indented to a 50 µm thickness and with a 150-200 µm holes were used. For all the experimental runs, a glovebox equipped with a microscope was used to load the samples in the gasket hole and then to seal the DAC with screws at the lowest pressure achievable. Alkali

salts, finely milled and stored in an oven at 120 °C, were used as pressure transmitting media (PTM): NaCl for XRD experiments and CsI for IR. These PTM ensure a good compromise between hydrostatic conditions and non-penetration of the medium inside the pores, as previously demonstrated.[20,38] The ruby fluorescence technique was used for the pressure measurement in the HP IR experiments while the NaCl equation of state was employed during XRD measurements.

HP XRD data were recorded at the CRISTAL beamline using a monochromatic beam (40x40 μm^2) with a wavelength of 0.5802 Å and a Rayonix SX165 detector. The Dioptas software was used to convert 2D diffraction images to 1D patterns.[39] Lattice parameters were extracted through a Le Bail refinement.

IR spectra at high pressure were acquired at the SMIS beamline using a Thermo-Fisher iS50 Fourier Transform IR interferometer coupled with synchrotron radiation. The DAC was placed between two long working distance custom Schwarzschild objectives in a home-built horizontal microscope. A liquid He cooled Si bolometer was used to collect far infrared (FIR) spectra in the 200-700 cm^{-1} spectral range while mid infrared (MIR) spectra, between 700-4000 cm^{-1}, were collected with a liquid N_2 cooled MCT/A detector. Peak frequencies have been obtained via least-square fitting using Lorentzian functions. For both experiments, pressure was increased at a rate of about 0.02 GPa per minute.

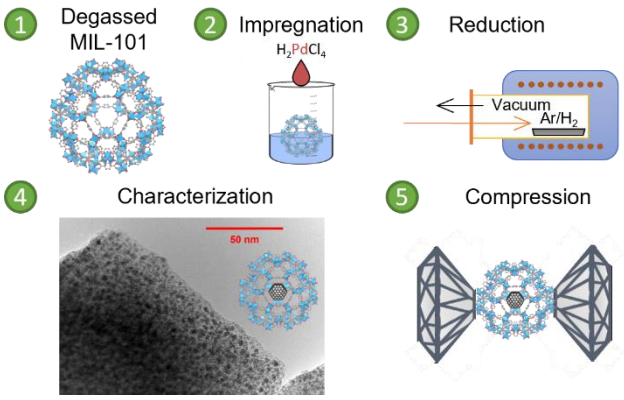

Figure 1. Scheme of the synthesis procedure and characterization of x-Pd@MIL-101 samples. The steps are the following: (1) degas of pristine MIL-101, (2) impregnation, (3) reduction, (4) characterization at ambient conditions and (5) high-pressure study using a diamond anvil cell.

RESULTS AND DISCUSSION

The 20-Pd@MIL-101 and 35-Pd@MIL-101 composites have been synthesized following a double-impregnation method, as previously detailed in the experimental section, and characterized by laboratory XRD measurements at ambient conditions, as shown in the Supporting Information (SI) in Figure S1-S2. The comparison between the XRD patterns of Pd doped and pristine samples clearly indicates that the NPs insertion does not alter the framework structure. The presence of Pd has been then verified by transmission electronic microscopy (TEM). The two samples show well distributed Pd NPs with narrow particles size distributions and average sizes of 1.1 (σ = 0.3) and 1.6 (σ = 0.5) nm, respectively, obtained from statistical analysis of NPs sizes (around 300) measured from several TEM images (Figure 2). It is worth noting that our synthetic procedure allows the preparation of Pd NPs with average size of 1.6 nm for very high metal loading (35 wt%), one of the highest for such small nanoparticles, to the best of our knowledge.[24] Isotherms obtained from N_2 adsorption/desorption measurements at Standard Temperature and Pressure

conditions (STP) for the two composites are shown in SI Figure S3 and correspond to curves typical of mesoporous materials, while the pore size distribution is shown in Figure S4. The specific surface area and the total pore volume decrease with the metal doping from 3549(±10) m^2/g to 1839(±10) m^2/g and 1388(±10) m^2/g and from 1.72(±0.01) cm^3/g to 0.86(±0.01) cm^3/g and 0.65(±0.01) cm^3/g for 20 wt% and 35 wt% Pd loading, respectively (see SI Table S1). This effect is due to the increase of sample density and to the presence of NPs which might hinder the N_2 adsorption into the pores.[32] Thermogravimetric analysis (TGA) was also performed on the synthesized samples and TGA curves are shown in Figure S5. Additional TEM figures are also provided in the SI (Figures S6-S11).

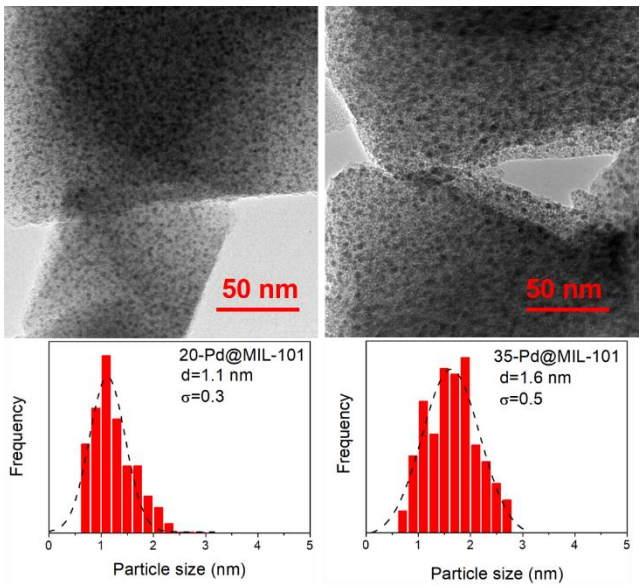

Figure 2. Selected TEM images with NPs size histograms of (left) 20-Pd@MIL-101 and (right) 35-Pd@MIL-101.

Selected XRD patterns at high-pressure for pristine MIL-101, 20-Pd@MIL-101 and 35-Pd@MIL-101 are displayed in Figure 3 in the low 2θ range, where the main diffraction peaks are observed.

The intensity MIL-101 peaks decreases as pressure increases and Bragg reflections become undetectable above 0.17 GPa. The original XRD pattern is not recovered after the pressure release (see Figure 3a) indicating that an irreversible amorphization occurs under compression below 0.17 GPa.[20] The two composites 20-Pd@MIL101 and 35-Pd@MIL-101 have a very different background as compared to the original MOF, especially at low 2θ (Figure 3-b,c). This is due to the strong scattering caused by the presence of Pd nanoparticles.[40] The full 2θ range is shown in SI Figure S12, where no diffraction peaks of the *fcc* Pd structure could be identified. This is due to the very short coherence length of ultra-small Pd NPs unable to diffract X-rays and also proves the absence of large Pd NPs agglomerated outside the pores, consistent with our earlier study on 20-Pd@MIL-101.[34]

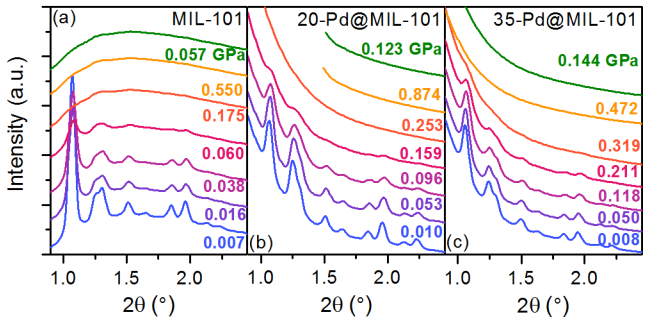

Figure 3. Selected powder XRD patterns (λ = 0.5802 Å) of (a) MIL-101, (b) 20-Pd@MIL-101 and (c) 35-Pd@MIL-101 under pressure. Patterns are vertically stacked for clarity. Data collected after pressure release are shown in green. In panel (b), data at 0.874 GPa and at 0.123 GPa (pressure released) are not available below about 1.5° due to the saturation of the detector.

Despite the different background, the evolution of the XRD patterns of the Pd doped samples qualitatively corresponds to the pressure response of pristine MIL-101. Bragg reflections weaken on compression becoming no longer detectable above a certain pressure value and they are not restored after the pressure release, thus indicating an irreversible pressure-induced amorphization

for both composites (see Figure 3-b,c). Detailed inspection reveals that the patterns of Pd loaded samples vanish at higher pressure compared with pristine MIL-101. The amorphization is completed around 0.25 GPa and 0.32 GPa for 20-Pd@MIL-101 and 35-Pd@MIL-101, respectively.

To quantify the differences in the structural response with and without Pd NPs, we performed a Le Bail refinement on the three datasets using the cubic $Fd\bar{3}m$ space group, as proposed originally by Férey in 2005.[41] In panel (a) of Figure 4, the unit cell volumes of pristine MIL-101, 20-Pd@MIL-101 and 35-Pd@MIL-101 are reported as a function of pressure up to 0.3 GPa. Each point has been normalized to the initial volume value obtained at the lowest pressure for each sample (the corresponding lattice parameters, not normalized, are given in the SI Figure S13). For the three samples, the unit cell volume shows a similar behavior under pressure, with an initial decrease then followed by a plateau. At higher pressures, the refinement is not possible due to the complete loss of Bragg reflections. From Figure 4a, it is noticeable that the slope, which is related to the compressibility of the material,[42] is affected by the amount of Pd NPs. To quantify this difference, we performed a fit of the experimental data with a second-order Birch-Murnaghan equation of state to obtain the bulk modulus of each sample, which is inversely related to the compressibility. The results are reported in Figure 4b and the fits of experimental points for the three samples are displayed in SI Figures S14-S16. The bulk modulus clearly increases with the metal loading, reaching an almost five-times larger value for the highest Pd content. The pressure value above which the volume compression ceases (*i.e.* the volume starts to be constant as function of pressure) is identified as the amorphization onset. The end of the volume compression on the crystalline phase, which gives the observed Bragg reflections, implies the concomitant nucleation of an amorphous phase.[20] The amorphization onset clearly shifts to higher pressure with increasing

Pd content from 0.05 GPa to 0.09 and 0.21 GPa for MIL-101, 20-Pd@MIL-101 and 35-Pd@MIL-101, respectively, as highlighted by the arrows in Figure 4a and shown in Figure 4c. The transition to the amorphous phase is completed at slightly higher pressure, when the XRD patterns are not present anymore, as previously discussed.

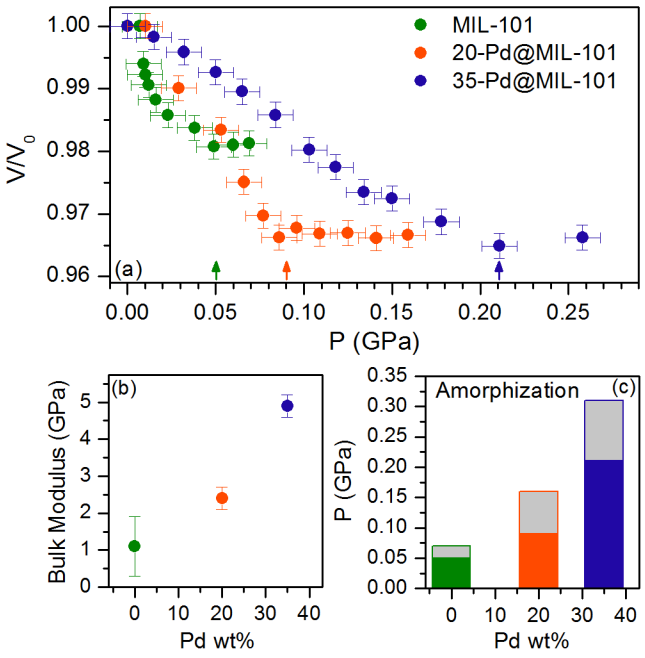

Figure 4. (a) Unit cell volume as a function of the pressure for pristine MIL-101 (green), 20-Pd@MIL-101 (orange) and 35-Pd@MIL-101 (blue) up to 0.3 GPa. Volume values are normalized to the lowest pressure values for each sample. (b) Relationship between the bulk modulus and the Pd loading. (c) Sketch of Pd content dependence of the amorphization pressure values. The grey part indicates the pressure range where the transition to the amorphous phase occurs.

To have complementary local information, we performed high-pressure synchrotron-based infrared spectroscopy on the Pd doped samples in the far-IR region. The FIR spectral evolution of the pressure response for 20-Pd@MIL-101 and 35-Pd@MIL-101 is shown in Figure 5. In this frequency range, the pristine MIL-101 presents two IR active modes, a collective mode (ν_1) at 389

cm^{-1}, tentatively assigned to an out-of-plane movement of the benzene ring coupled with a rocking of the metallic atom as proposed for MIL-53(Al),[43] and the other one around 589 cm^{-1} attributed to the CrO stretching in the metallic cluster (ν_2).[20,44] The IR spectra of x-Pd@MIL-101 samples closely resembles that of the pristine MIL-101[20] in the whole IR range (see SI Figure S17), with no apparent spectral modifications, indicating that no strong chemical interactions take place between the guest NPs and the host framework under pressure. In particular, the two OH modes at 3589 and 3671 cm^{-1} in x-Pd@MIL-101, which previously proved to be very sensitive to the presence of guest molecules,[20,45] present a line shape and pressure dependence similar to those measured for MIL-101 with the same solid PTM thus confirming the lack of guest-host chemical interactions.[20] When increasing pressure, the intensity of the ν_1 peak decreases in both 20-Pd@MIL-101 and 35-Pd@MIL-101, finally becoming hardly detectable above 0.6 GPa (see Figure 5). The ν_2 peak broadens but is observed in the whole pressure range, up to 1.0 GPa. It is worth noting that the OH modes detected around 3600 cm^{-1} become weaker under compression until they completely disappear at about 0.7 GPa (see SI Figure S17). These spectral modifications are not reversible after the pressure release, in agreement with XRD results.

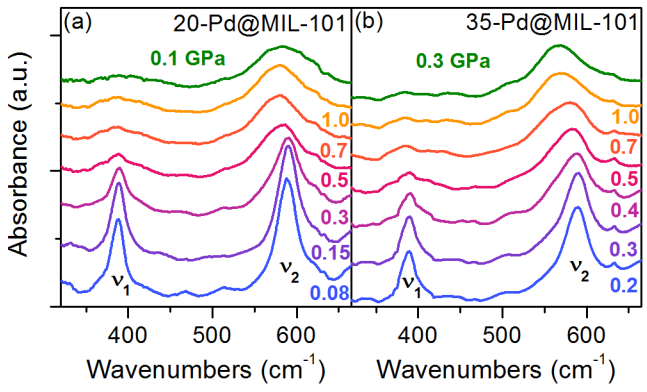

Figure 5. Selected FIR spectra of 20-Pd@MIL-101 (a) and 35-Pd@MIL-101 (b) measured under pressure. Spectra collected after the pressure release are shown in green. Spectra are vertically stacked for sake of clarity.

We quantified this observation by performing a least-square peak fitting using Lorentzian profiles of the x-Pd@MIL-101 spectra and pure MIL-101 previously published.[20] We obtained the peak heights - $h(\nu_i)$ - of both ν_1 and ν_2 modes, then used to calculate the $h(\nu_2)/ h(\nu_1)$ ratio at each pressure, shown in Figure 6a. This quantity is about 1.5 at the lowest pressure for the three samples, *i.e.* in the crystalline phase, and it stays constant until a pressure threshold, which depends on the Pd loading, is reached: 0.10(±0.05) GPa for MIL-101, 0.20(±0.05) GPa for 20-Pd@MIL-101, and 0.30(±0.05) GPa for 35-Pd@MIL-101. Above this threshold, the ratio monotonically increases with pressure until the ν_1 mode disappears. In Figure 6, the colored arrows indicate the pressure value where the crystal-to-amorphous phase transition is completed accordingly to XRD results. In summary, the collective mode intensity abruptly lowers compared to that of the CrO mode when the amorphization process is completed, as marked by the $h(\nu_2)/h(\nu_1)$ ratio deviation from the initial value of 1.5. This effect is clearly affected by the presence of Pd NPs, as found for the amorphization onset obtained from XRD.

From the peak fitting we also obtained the peak frequencies for both modes, as reported in Figure 6b-c up to 0.65 GPa. The ν_1 and ν_2 frequencies blue-shift in the pristine sample while a distinct behavior appears in the NPs doped samples, with a blue-shift followed by a red-shift as a function of pressure. The pressure value where this trend changes is affected by the metal loading, being 0.25 GPa for 20-Pd@MIL-101 and 0.4 for 35-Pd@MIL-101. This effect, once again, correlate well with the dependence of the crystalline-amorphous transition from the metal content observed by XRD. When the system is still crystalline with detectable Bragg reflections (see Figure 3), both

modes show a usual pressure-induced hardening, which reflects the reduction of interatomic distances.[42] On the contrary, the transition to the amorphous phase, *i.e.* the loss of long range order, is accompanied by the softening of these modes which suggest short-range instabilities or charge transfer effects.

The delayed disappearance of the collective ν_1 mode compared to the amorphization pressure value observed in XRD data indicates that short-range order is still present after the amorphization, at least in a narrow pressure range, and it is then completely lost for further compression. This is in agreement with a recent pair distribution function study on MIL-100(Fe) showing that short-range correlations are retained even in the amorphous phase obtained by ball milling treatment.[46]

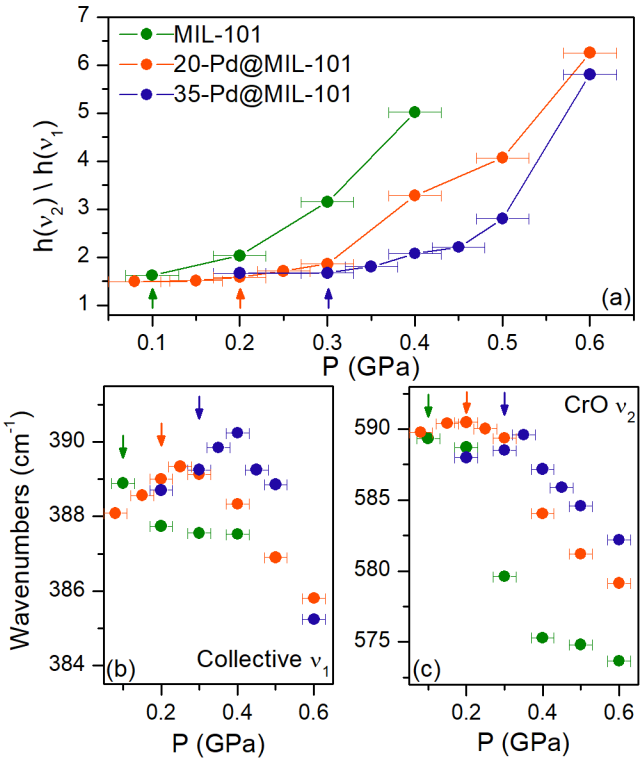

Figure 6. (a) Pressure dependence of the ratio between the peak heights of the ν_1 and ν_2 modes of MIL-101 (green), 20-Pd@MIL-101 (orange) and 35-Pd@MIL-101 (blue). Peak frequency of the

ν_1 (b) and ν_2 (c) modes as a function of pressure. Arrows highlight the pressure values where the amorphization is completed, as obtained from the XRD analysis.

In summary, XRD and IR data consistently show that embedding Pd nanoparticles inside the pores results in an increased mechanical stability of the framework. This phenomenon is likely due to steric effects of the Pd nanoparticles filling the pores since the stability range and the bulk moduli of the framework increase proportionally to the Pd loading. In our previous work we shown that the insertion of polymers into the pores of the pristine MIL-101 enhanced the framework stability by one order of magnitude but the control on the pore filling was lacking.[20] The present strategy, with its fine control of the metal loading inside the MOF, allows tuning, as demonstrated, the mechanical properties of the framework, indicating that the pore volume is gradually filled by Pd NPs increasing the metallic loading. The fact that the insertion inside MIL-101 of completely different chemicals, as a polymeric fluid and metallic NPs, increases the host's stability range confirms that the observed enhancement is mainly driven by a purely steric filling mechanism, where an ultimate "hyperfilling" of the pores is reached with the fluid. This also suggests that other host-guest interactions have little effect on the structural stability of MIL-101 under pressure.

Pd@MIL-101 composites thus result to be better candidates, compared to pristine MIL-101, for post-synthetic modification involving compression. Indeed, the shaping and densification of loose MOFs powders in pellets, beads or monoliths, which is necessary before any application, usually involves loadings up to several tons corresponding to pressures of hundreds of MPa,[47,48] *i.e.* values compatible with the pressure range explored in the present study. Therefore, combining the incorporation of functional nanomaterials in the framework with densification processing could become a successful strategy to further improve MOFs performances for applications. The enhanced stability of Pd@MIL-101 composites against the amorphization also represents new

evidence for the effective presence of Pd nanoparticles inside the pores which is often deduced exclusively from the compatibility of the average NPs size with the available pore diameters.

CONCLUSIONS

In this work, we have studied the effect of pressure on the mesoporous MIL-101 functionalized with Pd nanoparticles up to 35 wt% exploiting two complementary synchrotron-based techniques, X-ray diffraction and infrared spectroscopy. Such high metal loadings are achieved through a double solvent synthetic method and confirmed by laboratory techniques. The precise control of the NPs loading allowed us to show that the pressure value where the framework's amorphization process is completed shifts from about 0.1 GPa, for the pristine MIL-101, to around 0.3 GPa for the highest metal loading, *i.e.* 35 wt% Pd. The bulk modulus is also increased by the NPs presence, reaching nearly a fivefold increase for the 35-Pd@MIL-101 composite. From the infrared spectra, we identified a spectroscopic quantity tracking the amorphization process, *i.e.* the ratio between the heights of the peaks assigned to the chromium oxide stretching and the collective mode, which can be exploited from now on as a vibrational marker of the framework stability. The pressure dependence of the vibrational frequencies of the same IR modes suggests structural or electronic local effects on the chromium oxide clusters when the transition to the amorphous phase is completed. Both XRD and IR results show that increasing the Pd loading tunes the mechanical properties of the host framework enhancing its structural stability. This clearly points out that Pd nanoparticles are effectively inserted inside the MIL-101 pores, thus showing that the application of high mechanical pressure represents a powerful tool to demonstrate the successful insertion of well-dispersed nanometric objects inside MOFs' pores at least for high metal loadings. The enhancement of the mechanical stability of MIL-101 filled with Pd nanoparticles paves the way to

the quest of more stable, more functional MOFs for densification before gas absorption applications.

ASSOCIATED CONTENT

Supporting Information. Laboratory XRD patterns of as-synthesized samples MIL-101, 20-Pd@MIL-101 and 35-Pd@MIL-101 at ambient conditions. N_2 adsorption and desorption curves, BET surface area and pore volume values, pore size distributions, TGA curves, TEM images for each sample. DAC loading protocol. Full range XRD patterns of 20-Pd@MIL-101 and 35-Pd@MIL-101 under pressure. Pressure dependence of the lattice parameters. Second-order Birch-Murnaghan equation-of-state fits. MIR spectra of 35-Pd@MIL-101 at high pressure.

Notes

The authors declare no competing financial interests.

ACKNOWLEDGMENT

A.C, C.Z. and G.B. acknowledge the French National Research Agency (ANR) and the Romanian Ministry of Education and Research (UEFISCDI) for the financial support under MEMOS contract ANR-15-CE05-0012-01 and PN-II-ID-JRP-RO-FR-2015-0025, respectively. The authors gratefully acknowledge synchrotron SOLEIL (proposals #20200412 and # 20201415). A.C, A.P. and F.C. acknowledge the project CALIPSOplus (Grant Agreement 730872) from the EU Framework Programme for Research and Innovation HORIZON2020 for financial support for beamtimes at synchrotrons SOLEIL. Alain Polian and Abdelmalek Malouche are acknowledged for the help in the experimental preparation while Julie Bourgon and Junxian Zhang for performing

TEM and ICP-OES characterization. The authors thank A. Last from the Institute of Microstructure Technology of the Karlsruhe Nano-Micro Facility for providing a polymer x-ray lenses transfocator to horizontally focus the x-ray beam on the CRISTAL beamline. We also wish to thank Boby Joseph for preliminary measurements and support at Xpress beamline of ELETTRA synchrotron (proposal #20190313).

REFERENCES

(1) Yaghi, O. M.; O'Keeffe, M.; Ockwig, N. W.; Chae, H. K.; Eddaoudi, M.; Kim, J. Reticular Synthesis and the Design of New Materials. *Nature* **2003**, *423* (6941), 705–714. https://doi.org/10.1038/nature01650.

(2) Li, H.; Li, L.; Lin, R.-B.; Zhou, W.; Zhang, Z.; Xiang, S.; Chen, B. Porous Metal-Organic Frameworks for Gas Storage and Separation: Status and Challenges. *EnergyChem* **2019**, *1* (1), 100006. https://doi.org/10.1016/j.enchem.2019.100006.

(3) Wang, Y.; Yan, J.; Wen, N.; Xiong, H.; Cai, S.; He, Q.; Hu, Y.; Peng, D.; Liu, Z.; Liu, Y. Metal-Organic Frameworks for Stimuli-Responsive Drug Delivery. *Biomaterials* **2020**, *230*, 119619. https://doi.org/10.1016/j.biomaterials.2019.119619.

(4) Howarth, A. J.; Liu, Y.; Li, P.; Li, Z.; Wang, T. C.; Hupp, J. T.; Farha, O. K. Chemical, Thermal and Mechanical Stabilities of Metal–Organic Frameworks. *Nat. Rev. Mater.* **2016**, *1* (3), 1–15. https://doi.org/10.1038/natrevmats.2015.18.

(5) Healy, C.; Patil, K. M.; Wilson, B. H.; Hermanspahn, L.; Harvey-Reid, N. C.; Howard, B. I.; Kleinjan, C.; Kolien, J.; Payet, F.; Telfer, S. G.; Kruger, P. E.; Bennett, T. D. The Thermal Stability of Metal-Organic Frameworks. *Coord. Chem. Rev.* **2020**, *419*, 213388. https://doi.org/10.1016/j.ccr.2020.213388.

(6) Redfern, L. R.; Farha, O. K. Mechanical Properties of Metal–Organic Frameworks. *Chem. Sci.* **2019**, *10* (46), 10666–10679. https://doi.org/10.1039/C9SC04249K.

(7) Collings, I. E.; Goodwin, A. L. Metal–Organic Frameworks under Pressure. *J. Appl. Phys.* **2019**, *126* (18), 181101. https://doi.org/10.1063/1.5126911.

(8) McKellar, S. C.; Moggach, S. A. Structural Studies of Metal–Organic Frameworks under High Pressure. *Acta Crystallogr. Sect. B Struct. Sci. Cryst. Eng. Mater.* **2015**, *71* (6), 587–607. https://doi.org/10.1107/S2052520615018168.

(9) Serra-Crespo, P.; Dikhtiarenko, A.; Stavitski, E.; Juan-Alcañiz, J.; Kapteijn, F.; Coudert, F.-X.; Gascon, J. Experimental Evidence of Negative Linear Compressibility in the MIL-53 Metal–Organic Framework Family. *CrystEngComm* **2014**, *17* (2), 276–280. https://doi.org/10.1039/C4CE00436A.

(10) Cai, W.; Katrusiak, A. Giant Negative Linear Compression Positively Coupled to Massive Thermal Expansion in a Metal–Organic Framework. *Nat. Commun.* **2014**, *5* (1), 4337. https://doi.org/10.1038/ncomms5337.

(11) Cairns, A. B.; Catafesta, J.; Levelut, C.; Rouquette, J.; van der Lee, A.; Peters, L.; Thompson, A. L.; Dmitriev, V.; Haines, J.; Goodwin, A. L. Giant Negative Linear Compressibility in Zinc Dicyanoaurate. *Nat. Mater.* **2013**, *12* (3), 212–216. https://doi.org/10.1038/nmat3551.

(12) Connolly, B. M.; Madden, D. G.; Wheatley, A. E. H.; Fairen-Jimenez, D. Shaping the Future of Fuel: Monolithic Metal–Organic Frameworks for High-Density Gas Storage. *J. Am. Chem. Soc.* **2020**, *142* (19), 8541–8549. https://doi.org/10.1021/jacs.0c00270.
(13) Nandasiri, M. I.; Jambovane, S. R.; McGrail, B. P.; Schaef, H. T.; Nune, Satish. K. Adsorption, Separation, and Catalytic Properties of Densified Metal-Organic Frameworks. *Coord. Chem. Rev.* **2016**, *311*, 38–52. https://doi.org/10.1016/j.ccr.2015.12.004.
(14) Blanita, G.; Coldea, I.; Misan, I.; Lupu, D. Hydrogen Cryo-Adsorption by Hexagonal Prism Monoliths of MIL-101. *Int. J. Hydrog. Energy* **2014**, *39* (30), 17040–17046. https://doi.org/10.1016/j.ijhydene.2014.08.038.
(15) Ardelean, O.; Blanita, G.; Borodi, G.; Lazar, M. D.; Misan, I.; Coldea, I.; Lupu, D. Volumetric Hydrogen Adsorption Capacity of Densified MIL-101 Monoliths. *Int. J. Hydrog. Energy* **2013**, *38* (17), 7046–7055. https://doi.org/10.1016/j.ijhydene.2013.03.161.
(16) Oh, H.; Lupu, D.; Blanita, G.; Hirscher, M. Experimental Assessment of Physical Upper Limit for Hydrogen Storage Capacity at 20 K in Densified MIL-101 Monoliths. *RSC Adv.* **2013**, *4* (6), 2648–2651. https://doi.org/10.1039/C3RA46233A.
(17) Samantaray, S. S.; Putnam, S. T.; Stadie, N. P. Volumetrics of Hydrogen Storage by Physical Adsorption. *Inorganics* **2021**, *9* (6), 45. https://doi.org/10.3390/inorganics9060045.
(18) Hou, J.; Sapnik, A. F.; Bennett, T. D. Metal–Organic Framework Gels and Monoliths. *Chem. Sci.* **2020**, *11* (2), 310–323. https://doi.org/10.1039/C9SC04961D.
(19) Hong, W. Y.; Perera, S. P.; Burrows, A. D. Manufacturing of Metal-Organic Framework Monoliths and Their Application in CO2 Adsorption. *Microporous Mesoporous Mater.* **2015**, *214*, 149–155. https://doi.org/10.1016/j.micromeso.2015.05.014.
(20) Celeste, A.; Paolone, A.; Itié, J.-P.; Borondics, F.; Joseph, B.; Grad, O.; Blanita, G.; Zlotea, C.; Capitani, F. Mesoporous Metal–Organic Framework MIL-101 at High Pressure. *J. Am. Chem. Soc.* **2020**, *142* (35), 15012–15019. https://doi.org/10.1021/jacs.0c05882.
(21) Liu, D.; Zou, D.; Zhu, H.; Zhang, J. Mesoporous Metal–Organic Frameworks: Synthetic Strategies and Emerging Applications. *Small* **2018**, *14* (37), 1801454. https://doi.org/10.1002/smll.201801454.
(22) Yu, J.; Mu, C.; Yan, B.; Qin, X.; Shen, C.; Xue, H.; Pang, H. Nanoparticle/MOF Composites: Preparations and Applications. *Mater. Horiz.* **2017**, *4* (4), 557–569. https://doi.org/10.1039/C6MH00586A.
(23) Zlotea, C.; Campesi, R.; Cuevas, F.; Leroy, E.; Dibandjo, P.; Volkringer, C.; Loiseau, T.; Férey, G.; Latroche, M. Pd Nanoparticles Embedded into a Metal-Organic Framework: Synthesis, Structural Characteristics, and Hydrogen Sorption Properties. *J. Am. Chem. Soc.* **2010**, *132* (9), 2991–2997. https://doi.org/10.1021/ja9084995.
(24) Malouche, A.; Zlotea, C.; Szilágyi, P. Á. Interactions of Hydrogen with Pd@MOF Composites. *ChemPhysChem* **2019**, *20* (10), 1282–1295. https://doi.org/10.1002/cphc.201801092.
(25) Yang, Q.; Xu, Q.; Jiang, H.-L. Metal–Organic Frameworks Meet Metal Nanoparticles: Synergistic Effect for Enhanced Catalysis. *Chem. Soc. Rev.* **2017**, *46* (15), 4774–4808. https://doi.org/10.1039/C6CS00724D.
(26) Hu, Y.; Liao, J.; Wang, D.; Li, G. Fabrication of Gold Nanoparticle-Embedded Metal–Organic Framework for Highly Sensitive Surface-Enhanced Raman Scattering Detection. *Anal. Chem.* **2014**, *86* (8), 3955–3963. https://doi.org/10.1021/ac5002355.

(27) Falcaro, P.; Ricco, R.; Yazdi, A.; Imaz, I.; Furukawa, S.; Maspoch, D.; Ameloot, R.; Evans, J. D.; Doonan, C. J. Application of Metal and Metal Oxide Nanoparticles@MOFs. *Coord. Chem. Rev.* **2016**, *307*, 237–254. https://doi.org/10.1016/j.ccr.2015.08.002.
(28) Chen, G.; Wu, S.; Liu, H.; Jiang, H.; Li, Y. Palladium Supported on an Acidic Metal-Organic Framework as an Efficient Catalyst in Selective Aerobic Oxidation of Alcohols. *Green Chem* **2013**, *15* (1), 230–235. https://doi.org/10.1039/C2GC36618E.
(29) Rosler, C.; Fischer, R. A. Metal-Organic Frameworks as Hosts for Nanoparticles. *CrystEngComm* **2015**, *17* (2), 199–217. https://doi.org/10.1039/C4CE01251H.
(30) Lewis, F. A. The Palladium-Hydrogen System A SURVEY OF HYDRIDE FORMATION AND THE EFFECTS OF HYDROGEN CONTAINED WITHIN THE METAL LATTICES. *Platinum. Met. Rev.* **1982**, No. 26, 121–128.
(31) Biffis, A.; Centomo, P.; Del Zotto, A.; Zecca, M. Pd Metal Catalysts for Cross-Couplings and Related Reactions in the 21st Century: A Critical Review. *Chem. Rev.* **2018**, *118* (4), 2249–2295. https://doi.org/10.1021/acs.chemrev.7b00443.
(32) Chen, D.; Yang, W.; Jiao, L.; Li, L.; Yu, S.-H.; Jiang, H.-L. Boosting Catalysis of Pd Nanoparticles in MOFs by Pore Wall Engineering: The Roles of Electron Transfer and Adsorption Energy. *Adv. Mater.* **2020**, *32* (30), 2000041. https://doi.org/10.1002/adma.202000041.
(33) Chen, L.; Xu, Q. Metal-Organic Framework Composites for Catalysis. *Matter* **2019**, *1* (1), 57–89. https://doi.org/10.1016/j.matt.2019.05.018.
(34) Malouche, A.; Blanita, G.; Lupu, D.; Bourgon, J.; Nelayah, J.; Zlotea, C. Hydrogen Absorption in 1 Nm Pd Clusters Confined in MIL-101(Cr). *J. Mater. Chem. A* **2017**. https://doi.org/10.1039/C7TA07159K.
(35) Chen, Y.-Z.; Gu, B.; Uchida, T.; Liu, J.; Liu, X.; Ye, B.-J.; Xu, Q.; Jiang, H.-L. Location Determination of Metal Nanoparticles Relative to a Metal-Organic Framework. *Nat. Commun.* **2019**, *10* (1), 3462. https://doi.org/10.1038/s41467-019-11449-6.
(36) Houk, R. J. T.; Jacobs, B. W.; Gabaly, F. E.; Chang, N. N.; Talin, A. A.; Graham, D. D.; House, S. D.; Robertson, I. M.; Allendorf, M. D. Silver Cluster Formation, Dynamics, and Chemistry in Metal−Organic Frameworks. *Nano Lett.* **2009**, *9* (10), 3413–3418. https://doi.org/10.1021/nl901397k.
(37) Blăniţă, G.; Lupu, D.; Grad, O.; Misan, I.; Coldea, I.; Borodi, G. Synthetic Method of MIL-101(Cr) Metal-Organic Framework. 132757 A0.
(38) Celeste, A.; Borondics, F.; Capitani, F. Hydrostaticity of Pressure-Transmitting Media for High Pressure Infrared Spectroscopy. *High Press. Res.* **2019**, *39* (4), 608–618. https://doi.org/10.1080/08957959.2019.1666844.
(39) Prescher, C.; Prakapenka, V. B. DIOPTAS: A Program for Reduction of Two-Dimensional X-Ray Diffraction Data and Data Exploration. *High Press. Res.* **2015**, *35* (3), 223–230. https://doi.org/10.1080/08957959.2015.1059835.
(40) Li, T.; Senesi, A. J.; Lee, B. Small Angle X-Ray Scattering for Nanoparticle Research. *Chem. Rev.* **2016**, *116* (18), 11128–11180. https://doi.org/10.1021/acs.chemrev.5b00690.
(41) Férey, G.; Mellot-Draznieks, C.; Serre, C.; Millange, F.; Dutour, J.; Surblé, S.; Margiolaki, I. A Chromium Terephthalate-Based Solid with Unusually Large Pore Volumes and Surface Area. *Science* **2005**, *309* (5743), 2040–2042.
(42) Bini, R.; Schettino, V. *Materials Under Extreme Conditions - Molecular Crystals at High Pressure*; Imperial College Press, 2013.

(43) Hoffman, A. E. J.; Vanduyfhuys, L.; Nevjestić, I.; Wieme, J.; Rogge, S. M. J.; Depauw, H.; Van Der Voort, P.; Vrielinck, H.; Van Speybroeck, V. Elucidating the Vibrational Fingerprint of the Flexible Metal–Organic Framework MIL-53(Al) Using a Combined Experimental/Computational Approach. *J. Phys. Chem. C* **2018**, *122* (5), 2734–2746. https://doi.org/10.1021/acs.jpcc.7b11031.

(44) Hadjiivanov, K. I.; Panayotov, D. A.; Mihaylov, M. Y.; Ivanova, E. Z.; Chakarova, K. K.; Andonova, S. M.; Drenchev, N. L. Power of Infrared and Raman Spectroscopies to Characterize Metal-Organic Frameworks and Investigate Their Interaction with Guest Molecules. *Chem. Rev.* **2021**, *121* (3), 1286–1424. https://doi.org/10.1021/acs.chemrev.0c00487.

(45) Volkringer, C.; Leclerc, H.; Lavalley, J.-C.; Loiseau, T.; Férey, G.; Daturi, M.; Vimont, A. Infrared Spectroscopy Investigation of the Acid Sites in the Metal–Organic Framework Aluminum Trimesate MIL-100(Al). *J. Phys. Chem. C* **2012**, *116* (9), 5710–5719. https://doi.org/10.1021/jp210671t.

(46) F. Sapnik, A.; N. Johnstone, D.; M. Collins, S.; Divitini, G.; M. Bumstead, A.; W. Ashling, C.; A. Chater, P.; S. Keeble, D.; Johnson, T.; A. Keen, D.; D. Bennett, T. Stepwise Collapse of a Giant Pore Metal–Organic Framework. *Dalton Trans.* **2021**, *50* (14), 5011–5022. https://doi.org/10.1039/D1DT00881A.

(47) Yuan, S.; Sun, X.; Pang, J.; Lollar, C.; Qin, J.-S.; Perry, Z.; Joseph, E.; Wang, X.; Fang, Y.; Bosch, M.; Sun, D.; Liu, D.; Zhou, H.-C. PCN-250 under Pressure: Sequential Phase Transformation and the Implications for MOF Densification. *Joule* **2017**, *1* (4), 806–815. https://doi.org/10.1016/j.joule.2017.09.001.

(48) Wang, T. C.; Wright, A. M.; Hoover, W. J.; Stoffel, K. J.; Richardson, R. K.; Rodriguez, S.; Flores, R. C.; Siegfried, J. P.; Vermeulen, N. A.; Fuller, P. E.; Weston, M. H.; Farha, O. K.; Morris, W. Surviving Under Pressure: The Role of Solvent, Crystal Size, and Morphology During Pelletization of Metal–Organic Frameworks. *ACS Appl. Mater. Interfaces* **2021**, *13* (44), 52106–52112. https://doi.org/10.1021/acsami.1c09619.